JOURNAL OF Materials CHEMISTRY

Synthesis, structure, electrical and magnetic properties of the new non-stoichiometric perovskite phase, Ca_2MnNbO_γ

Angela Kruth,[a] Mitsuharu Tabuchi,[b] Ulrich Guth[c] and Anthony R. West[a]

[a]*University of Aberdeen, Department of Chemistry, Meston Walk, Aberdeen, UK AB24 3UE*
[b]*Osaka National Research Institute, 1-8-31 Midorigaoka, Ikeda, Osaka 563, Japan*
[c]*University of Greifswald, Department of Chemistry, Institute of Physical Chemistry, Soldtmannstraße 23, 17489 Greifswald, Germany*

Received 26 June 1998, Accepted 6th August 1998

The new phase Ca_2MnNbO_γ has an orthorhombic, $GdFeO_3$ structure with B site disorder of Mn and Nb. The oxygen content γ varies from 5.86 to 6.00 depending on heat treatment conditions. Treatment in high pressure O_2 is required for full oxidation. Magnetic susceptibility measurements indicate mixed valence (2+, 3+) of Mn for $\gamma = 5.87$ and Curie–Weiss paramagnetism at high temperatures. SQUID measurements indicate spin glass-like behaviour below 15 K. Ac impedance shows semiconducting behaviour, $E = 0.31(2)$ eV. On heating in O_2-poor atmospheres, resistive surface layers and grain boundary effects are seen, which point to a p-type conduction mechanism.

Introduction

Perovskites and perovskite-related oxides offer a wide range of interesting electrical properties, *e.g.* giant magnetoresistance, superconductivity and oxide ion conductivity. Mixed oxide ion–electron conducting perovskites have possible uses as electrode materials in oxygen sensors and solid-oxide fuel cells and may have major advantages over porous noble-metal electrodes because they are stable to temperatures well above 1250 °C[1] and charge-transfer reactions can take place everywhere at the electrode/gas interface, rather than at the triple junctions: electrolyte/electrode/gas. In some non-stoichiometric perovskites, electrochemical reactions occur at specific vacant surface sites;[2–4] these materials exhibit catalytic activity for processes such as the oxidation of CH_x and NO_x.

Perovskites based on elements of the first transition series display a wide variety of defect-related phenomena which have their origin in the unfilled 3d electron shell. The relative ease with which electrons can be removed from or added to some metals, especially Fe and Mn, means that they often exist in numerous valence states, depending on temperature and oxygen partial pressure; this also gives rise to a potentially large number of phases, which themselves may deviate from exact stoichiometry in terms of both cation and oxygen content.[5] Non-stoichiometry was until recently explained in terms of point defect equilibria.[6,7] For most compounds with sizeable deviations (>1%) in stoichiometry, however, the concept of point defect equilibria is inadequate. Alternative models are needed which involve ordering of point defects or new structural features which eliminate point defects.[8] Defects in perovskite oxides can arise from cation deficiency in either A or B sites or oxygen deficiency; the resulting vacancies often form ordered superstructures.

Tofield and Scott[9] suggested three possible models to accommodate oxygen excess in the perovskite structure: (*i*) introduction of interstitial oxygen at either $(\frac{1}{2}00)$ or $(\frac{1}{4}\frac{1}{4}\frac{1}{4})$ positions of the cubic unit cell; this, however, is energetically unfavourable; (*ii*) creation of cation vacancies at A and/or B sites, leaving a perfect oxygen sublattice and (*iii*) formation of new, oxidised perovskite-related phases. For example, in $LaMnO_{3+\lambda}$ and $La_2TiCoO_{6+\lambda}$, oxygen excess is accommodated by vacancies in both A and B sites.[10,11] In $Cu_2Nb_2O_7$ and $La_2Ti_2O_7$ with large oxygen excess, new perovskite-related structures form: the parent, cubic perovskite is sliced parallel to (110) to give slabs of composition $(A_{n-1}B_nO_{3n+2})_\infty$ which stack together with a layer of A-atoms in between. A homologous series, $A_nB_nO_{3n+2}$ forms, with $n=4$ in this case, but in other phases *n*-values range from 1 to 6.[12–14] The brownmillerite structure of $Ca_2Fe_2O_5$ and Ca_2FeAlO_5 is derived from perovskite with ordering of oxygen vacancies.[15,16] The oxygen vacancies give tetrahedral coordination of iron resulting in alternate sheets of FeO_6 octahedra and FeO_4 tetrahedra. $CaMnO_{3-\delta}$ also has oxygen vacancies, in the compositional range $0 \leqslant \delta \leqslant 0.5$, which order at certain compositions; Mn has mixed 3+/4+ valence and occupies a mixture of octahedra and square-pyramids which form ordered intergrowth structures where the proportion of square-pyramidal Mn^{3+} relative to octahedral Mn^{4+} increases with δ. In $CaMnO_{2.5}$, $\delta = 0.5$, the Mn is 3+ and in five-fold square-pyramidal coordination only, which is distinct from brownmillerite which contains a mixture of tetrahedra and octahedra.[17,18]

On replacing Fe^{3+} in brownmillerite, $Ca_2Fe_2O_5$, by Nb^{5+}, an extensive oxygen-deficient, cubic perovskite solid solution, $Ca_2Fe_{2-x}Nb_xO_\gamma$: $0.45 \leqslant x \leqslant 0.65$ was obtained.[19] Its oxygen content is variable, *e.g.* $5.55 \leqslant \gamma \leqslant 5.92$ for $x = 0.6$. It has high electronic conductivity and probably also has high oxide ion conductivity since the oxygen content, γ, readjusts rapidly on varying either temperature or oxygen partial pressure and could therefore have uses as a mixed conducting electrode in devices involving gas–solid interfacial reactions.

This project is based on the $Ca_2Fe_2O_5$–$CaMnO_3$–$Ca_2Nb_2O_7$ system with the initial objective of synthesising perovskite-related phases with variable oxygen content, high mixed electronic and oxide ion conductivities and stability under both reducing and oxidising conditions over large temperature ranges. We attempt to control the oxidation state of Fe, Mn and associated oxygen content by both adjusting the niobium concentration at B-cation sites and post-reaction heat treatments at different oxygen pressures. Initial investigations were carried out on the binary joins, $Ca_2Fe_{1.4-x}Mn_xNb_{0.6}O_\gamma$ and $Ca_2Mn_{2-x}Nb_xO_\gamma$. As a first step, a variety of characterisation studies on the new phase, $Ca_2Mn_{2-x}Nb_xO_\gamma$ with $x = 1.0$, were made and are described here.

Experimental

Starting materials $CaCO_3$ (99%, AnalaR) and Nb_2O_5 (99.9%, Aldrich) were dried at 200 and 600 °C, respectively. MnO_2 (99%, Aldrich) was used directly from the bottle since a

thermogravimetry (TG) study confirmed its stoichiometry, during a two-stage decomposition to Mn_2O_3 at *ca.* 400–700 °C and Mn_3O_4 at *ca.* 900–1000 °C. Appropriate quantities of MnO_2, $CaCO_3$ and Nb_2O_5 giving *ca.* 5 g total weight were mixed in acetone for at least 10 minutes, dried and heated in Pt boats at 900 °C for 12 h, 1200 °C for 20 h and at 1200 °C to 1350 °C in steps of 50 °C for periods of 20 h each, with regrinding between each heating period. Samples were finally heated at 1400 °C for 72 h.

To modify the oxygen stoichiometry, samples were heated at different temperatures in air, O_2 or Ar and either quenched or cooled slowly to room temperature. A Morris High Pressure Furnace, HPS-3210 was used to anneal samples, wrapped in Au foil, under high O_2 pressure. Two experimental conditions were used which gave pressures at 600 °C of either *ca.* 40 or *ca.* 60 atm. After heating at 600 °C for 10 h, samples were cooled slowly under pressure.

Oxygen contents and the oxidation state of Mn were determined from a combination of TG and magnetic measurements. By TG, the oxygen contents were determined from the weight loss on reduction in 10% H_2–90% N_2 using a Stanton Redcroft TG-DTA 1500 instrument. A Shimadzu MB-3 magnetic balance was used to measure magnetic susceptibility values which were converted to effective magnetic moments and then compared with theoretical values obtained from the 'spin-only' formula: $(NH_4)_2Mn(SO_4)_2{\cdot}6H_2O$ was used as calibration standard. SQUID measurements were carried out below 100 K with magnetic fields of 5000 and 10 Oe.

Phase identity, stability and purity were determined by powder X-ray diffraction, Hägg-Guinier camera, Cu-Kα_1 radiation. For indexing and lattice parameter refinement, a Philips Diffractometer PW1710 and Stoe Stadi P software were used, KCl internal standard, 20 to 80° 2θ, Cu-Kα_1 radiation. A Stoe Stadi P transmission diffractometer was used for structural studies (Rietveld refinement) of the fully oxidized phase, Ca_2MnNbO_6 with data collected over the range 8 to 113° 2θ and step width 0.02°. The refinement was carried out using the package PFSR (pattern–fitting structure–refinement) with programs CDF, CDE, RVI and RVR. First, the lattice parameters and halfwidths of the reflections were refined, *e.g.* lattice constants, 2θ zero point, halfwidth parameters and background. After convergence of profile refinement, the structural parameters were refined, *e.g.* overall scale factor, atomic coordinates and isotropic thermal vibration parameters. DTA was used to look for any phase transitions over the range 25 to 1300 °C in air, at heating and cooling rates of 8 K min^{-1}.

Electrical properties in air over the range −60 to 200 °C were determined by ac impedance spectroscopy over the frequency range 0.03 Hz to 13 MHz using a Hewlett-Packard 4192A LF Impedance Analyser. Pellets, 8 mm diameter and 1–2 mm thick, were prepared by cold-pressing powders at *ca.* 200 MPa, sintered in air overnight at 1400 °C and quenched to room temperature. To modify the oxygen content, pellets were heated at 1100 °C for 5 h and slowly cooled to room temperature (2 K min^{-1}) in either O_2 or N_2. One pellet was annealed at 600 °C and *ca.* 40 atm O_2. Electrodes were attached by coating pellet faces with a thin InGa (1 : 1) alloy layer and gold strips held to the sample by pressure.

Results and discussion

The new phase, Ca_2MnNbO_γ, was obtained on reaction of the oxides in a stepwise heating programme; phase-pure samples were obtained finally after heating at 1400 °C, 72 h. This new phase was easily recognised since its XRD pattern is very similar to that of Ca_2FeNbO_6[19] and, therefore, it also has an orthorhombic, $GdFeO_3$ structure.

Oxygen contents, γ, were determined by H_2-reduction TG; typical traces are shown in Fig. 1. In all cases, no reduction occurred up to at least 400 °C but reduction was complete by 950–1150 °C. Samples with higher oxygen contents (c,d) started to lose weight at lower temperatures than the others.

Although weight losses could be determined accurately for all samples, in order to convert these to variations in oxygen content, it was necessary to know the stoichiometry of either the final, fully reduced state or that of at least one of the starting compositions. The assumption was made initially that the H_2-reduction would affect only the oxidation state of Mn and that the final state in all cases would be Mn^{2+}, corresponding to an overall final stoichiometry of '$Ca_2MnNbO_{5.5}$'; H_2 reduction of $CaMnO_{3-\delta}$ had shown the product to be $CaMnO_2$, containing Mn^{2+}[17] and we assumed a similar behaviour for our samples. Using this assumption, the starting compositions were evaluated. Two samples heated in high pressure O_2 had γ values close to 6, *viz.* 6.02(3) after 40 atm O_2 at 600 °C and 5.97(3) after 60 atm O_2; within errors, it is concluded that these were fully oxygenated with $\gamma = 6.00$. An oxygen content of 6 is the highest that can be expected for this structure type; a large number of phases with analogous formulae and $GdFeO_3$ structure are known and all have an oxygen content of $\leqslant 6$. This result therefore further supports the correctness of the initial assumption concerning the stoichiometry of the H_2-reduced samples.

The oxygen content of Ca_2MnNbO_δ varied according to the

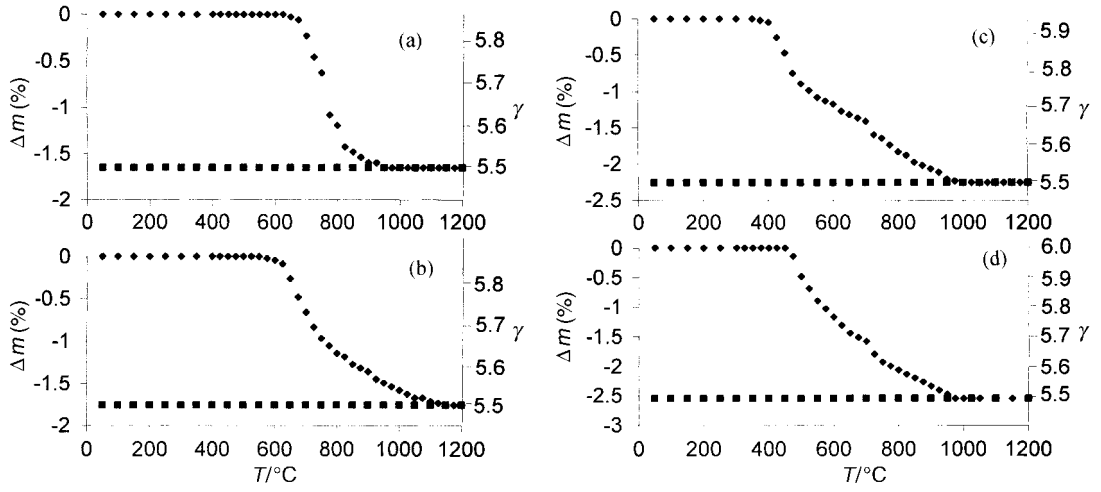

Fig. 1 Weight loss and corresponding oxygen content, γ, during H_2 reduction of samples prepared under different heating conditions: (a) slowly cooled from 1100 °C in Ar, (b) quenched from 1400 °C in air, (c) slowly cooled from 1100 °C in O_2 and (d) heated at *ca.* 40 atm O_2 and 600 °C; during heating ◆ and cooling ■ cycle.

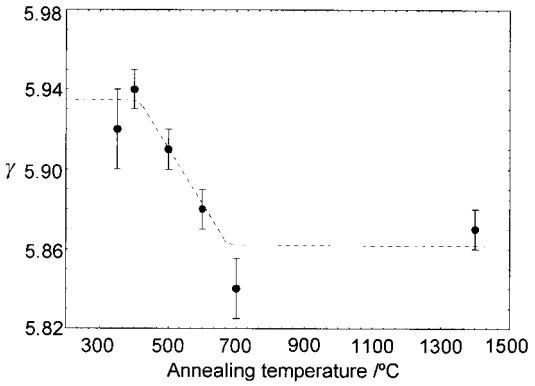

Fig. 2 Influence of annealing temperature in air on oxygen content, γ, in Ca_2MnNbO_γ.

final heat treatment conditions; lowest values were obtained at high temperatures, *e.g.* 5.87 in air at 1400 °C and 5.86 in Ar at 1200 °C. The oxygen content as a function of temperature in air is shown in Fig. 2. The data were obtained on samples quenched from different temperatures and show that oxygen content varies over the range *ca.* 400 to 700 °C but is essentially constant at higher and lower temperatures.

Indexed powder XRD data for one composition, $Ca_2MnNbO_{5.87}$, are given in Table 1. The data index on an orthorhombic unit cell with a $\sqrt{2}$, $\sqrt{2}$, 2 relation to a cubic perovskite-like subcell. Lattice parameters show a small increase in c with decreasing γ from 7.683 Å for $\gamma=6.00$ to 7.706 Å for $\gamma=5.87$; a and b change little with γ.

Ca_2MnNbO_6 for Rietveld refinement was synthesised in 60 atm oxygen. The starting model was the orthorhombic perovskite-related $GdFeO_3$ structure.[20] A Pearson VII profile function with exponent $m=2.0$ was applied. The profile and structural parameters allowed to refine were scale factor, 2θ zero point, cell constants, background, halfwidth polynomial, atomic positions for all atoms and thermal vibration parameters for Ca and Mn/Nb. After convergence, R-factors were: $R(p)=0.0343$, $R(wp)=0.0443$ and $R(I,hkl)=0.1332$. Final values for atomic positions and thermal parameters are given in Table 2 and Table 3 shows calculated Ca—O and Nb/Mn—O bond lengths. The XRD pattern for Ca_2MnNbO_6 and the difference between observed and calculated profiles are shown in Fig. 3.

Magnetic measurements were carried out for $Ca_2MnNbO_{5.87}$; Fig. 4(a) shows the field dependence of magnetization at 83 and 293 K between 1.8 and 12.5 kOe. No spontaneous magnetization was observed down to 83 K. The magnetic susceptibility was 4.17×10^{-5} cm^3 g^{-1}, which is sufficiently large to ignore the contribution of closed shell diamagnetism, 3.33×10^{-7} cm^3 g^{-1}. Temperature dependence of the inverse molar susceptibility, χ_m^{-1}, reveals a Curie–Weiss paramagnetism down to 83 K, Fig. 4(b), with $\mu_{eff}=5.341(6)\ \mu_B$ and $\theta=+21$ K. The positive Weiss temperature suggests ferromagnetic coupling below 83 K. The observed μ_{eff} value is intermediate between the spin only values of Mn^{2+}, $\mu_{eff,Mn2+}=\sqrt{35}\ \mu_B=5.92\ \mu_B$, and Mn^{3+}, $\mu_{eff,Mn3+}=\sqrt{24}\ \mu_B=4.90\ \mu_B$, suggesting that this sample is a $Mn^{2+/3+}$ mixed valence compound. This is consistent with the TG value for the oxygen content, $\gamma=5.87$, which gives a 26:74 ratio for $Mn^{2+}:Mn^{3+}$.

SQUID measurements made for two applied fields over the temperature range 4–100 K are shown in Fig. 5. Above 20 K, the data sets are essentially superposable but diverge dramatically at lower temperature. In particular, the zero field cooled data at 10 Oe show a sharp magnetisation maximum at 15 K which transforms to an almost temperature-independent magnetisation in field cooled data. Such features are strongly indicative of spin glass-like behaviour of the kind reported in

Table 1 X-Ray powder diffraction data for $Ca_2MnNbO_{5.87}$ orthorhombic; $a=5.4527(5)$ Å, $b=5.5622(5)$ Å, $c=7.7062(8)$ Å

h k l	Int.	*d*(obs)/Å	*d*(calc)/Å
1 1 0	30	3.8933	3.8938
0 0 2	14	3.8540	3.8531
1 1 1	3	3.4753	3.4753
0 2 0	25	2.7808	2.7811
1 1 2	100	2.7388	2.7388
2 0 0	25	2.7267	2.7263
2 1 0	2	2.4467	2.4481
1 2 1	2	2.3597	2.3586
2 1 1	3	2.3333	2.3332
1 0 3	2	2.3252	2.3236
1 1 3	2	2.1441	2.1442
1 2 2	2	2.0834	2.0839
2 1 2	2	2.0653	2.0663
2 2 0	25	1.9462	1.9469
0 0 4	13	1.9265	1.9266
2 2 1	3	1.8873	1.8876
1 3 0	4	1.7552	1.7554
2 2 2	5	1.7375	1.7377
1 1 4	6	1.7266	1.7268
1 3 1	2	1.7111	1.7115
1 3 2	12	1.5973	1.5974
0 2 4	8	1.5837	1.5837
3 1 2	22	1.5758	1.5764
2 0 4	16	1.5731	1.5734
1 3 3	1	1.4487	1.4493
0 4 0	2	1.3906	1.3905
2 2 4	10	1.3694	1.3694
4 0 0	3	1.3626	1.3632
3 2 3	2	1.3094	1.3091
4 1 1	1	1.3052	1.3049
3 3 0	2	1.2977	1.2979
4 0 2	2	1.2856	1.2851
2 4 0	1	1.2389	1.2387
3 3 2	3	1.2301	1.2300
2 4 1	3	1.2234	1.2230
0 4 3	6	1.2224	1.2229
1 1 6	3	1.2194	1.2197
2 4 2	4	1.1793	1.1793
4 2 2	4	1.1663	1.1666
0 2 6			1.1660
3 3 3	4	1.1584	1.1584
1 3 5			1.1582
0 4 4	2	1.1279	1.1275
4 0 4	2	1.1129	1.1128
1 5 2	4	1.0489	1.0488
2 4 4	2	1.0421	1.0419
1 3 6	2	1.0367	1.0365
4 2 4	6	1.0331	1.0331
5 1 2	4	1.0310	1.0311
3 1 6			1.0307

Fe analogue structures, A_2FeXO_6: A = Ca, Sr, Ba; X = Nb, Ti, Sb.[21–25]

Ac impedance data were recorded isothermally at temperatures in the range 200 to 400 K for pellets that had been given a range of post-sinter heat treatments. Two general patterns of behaviour were seen. Samples heat-treated in O_2-rich atmospheres showed the simplest response, Fig. 6 (a), (b); the Z'' *vs.* Z' complex plane plot showed a main arc and a much smaller, poorly-resolved, low frequency arc. Z'', M'' spectra showed essentially coincident peaks at high frequency with associated capacitance 8–10 pF, indicative of bulk or intragranular response. The low frequency Z'' shoulder peak had a capacitance of *ca.* 10 nF, attributable to either a thin surface layer or an electrode–sample interfacial effect. Hence, the impedance data were dominated by the bulk response of the sample and there is little evidence of resistive grain boundary effects (which would have capacitances in the range 0.1 to 1 nF).

For samples heated in air or N_2/Ar, the impedance response was more complex, Fig. 6(c), (d). The Z'' *vs.* Z' plots showed clear evidence of several overlapping arcs, but also dramatic

Table 2 Values for atomic coordinates and thermal vibration parameters for Ca_2MnNbO_6 in Rietveld refinement

Atom	Wyckoff position	Occ.	*x/a*	*y/b*	*z/c*	U_{ij}
Ca	4c	1.0	−0.0074(11)	0.0050(5)	0.2500	0.0150(1)
Mn	4b	0.5	0.5000	0.0000	0.0000	0.0025(4)
Nb	4b	0.5	0.5000	0.0000	0.0000	0.0025(4)
O(1)	4c	1.0	0.0915(15)	0.4684(19)	0.2500	0.0030
O(2)	8d	1.0	−0.2946(14)	0.2947(12)	0.04531(8)	0.0030

Table 3 Bond distances, *D*, and bond angles, α, for Ca_2MnNbO_6

Ca−O	*D*/Å		O−Mn/Nb−O	α/°
Ca−O(1)	2.303(10)	(1×)	O(2)−Mn/Nb−O(2)	87.5(3)
Ca−O(2)	2.358(7)	(2×)	O(2)−Mn/Nb−O(2)	89.0(3)
Ca−O(1)	2.416(11)	(1×)	O(2)−Mn/Nb−O(1)	89.3(3)
Ca−O(2)	2.618(8)	(2×)	O(2)−Mn/Nb−O(1)	90.7(3)
Ca−O(2)	2.700(7)	(2×)	O(2)−Mn/Nb−O(1)	91.0(3)
			O(2)−Mn/Nb−O(1)	92.5(3)
Mn/Nb−O	*D*/Å			
Mn/Nb−O(1)	1.992(2)	(2×)		
Mn/Nb−O(2)	1.999(7)	(2×)		
Mn/Nb−O(2)	2.013(7)	(2×)		

Pbnm (no. 62); $a=5.445$ Å, $b=5.555$ Å, $c=7.683$ Å. $R(p)=0.0343$, $R(wp)=0.0443$, $R(I,hkl)=0.1332$.

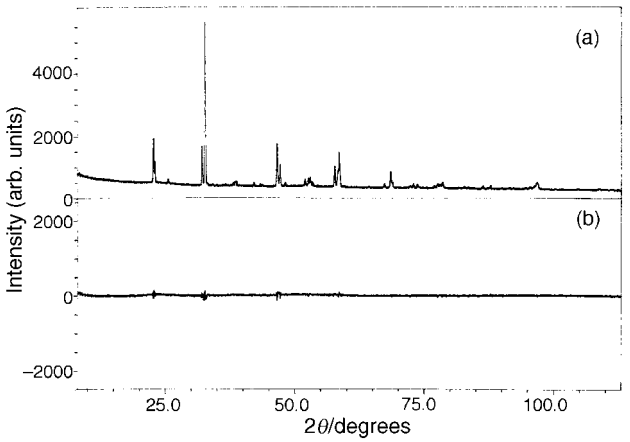

Fig. 3 Rietveld refinement: (a) observed pattern and (b) difference between observed and calculated patterns.

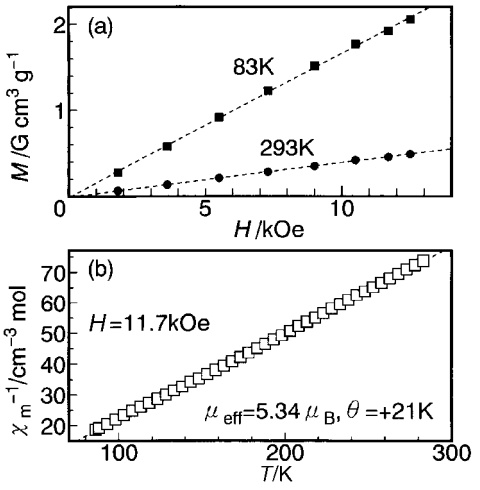

Fig. 4 Magnetic data for $Ca_2MnNbO_{5.87}$: (a) field dependence of magnetization and (b) Curie–Weiss plot.

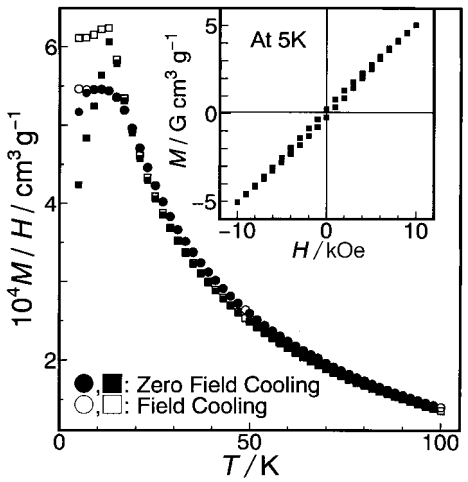

Fig. 5 SQUID measurement for $Ca_2MnNbO_{5.87}$: at 10 (■; □) and 5000 Oe (●; ○).

changes occurred on polishing the pellet surfaces prior to attaching electrodes (c). The bulk response was again seen at highest frequencies in the *M″* spectra, as the low frequency tail of a peak at $\geqslant 10^7$ Hz (d), but the corresponding *Z″* spectra and therefore the *Z″ vs. Z′* plots were completely dominated by large, lower frequency impedances. The sensitivity of the impedance response to polishing suggests that resistive surface layers are present, even after polishing; however, there is a large impedance, attributable to grain boundaries from its capacitance value of *ca.* 0.2 nF, which dominates the overall sample impedance. The conclusion from these observations is that resistive grain boundaries and surface layers appear on heating samples in less oxidising atmospheres.

In order to assess possible variation in bulk resistance as a consequence of different heat treatments, data for the frequency maxima in the *M″* spectra are compared in Fig. 7. A major advantage of comparing f_{max} data for a range of samples is that f_{max} is independent of sample geometry: *R* and *C* are both influenced by geometry, but inversely to each other and therefore, the geometrical terms cancel in f_{max}.[26] In addition, *C* values vary little from sample to sample for the bulk response of similar-sized pellets. Hence f_{max}, given by $2\pi f_{max}RC=1$, provides a direct measure of R^{-1} and hence of σ.

The data for four different heat treatments fall on a single straight line with activation energy 0.31(2) eV. This suggests that the bulk conduction mechanism, the conducting species and the magnitude of the conductivity are essentially independent of oxygen content for this range of compositions. Given the complete absence of any electrode polarisation effects in the low frequency region of the impedance response and the low value of the activation energy, it is concluded that the conduction species are electrons rather than ions, and therefore are associated with the mixed valency of Mn.

Conductivity data were extracted from the f_{max} data. These are plotted in Arrhenius format in Fig. 8, together with total pellet conductivity values, obtained from the low frequency intercepts of the *Z″ vs. Z′* plots on the *Z′* axis. The pellet conductivity values show a large variation, unlike the bulk

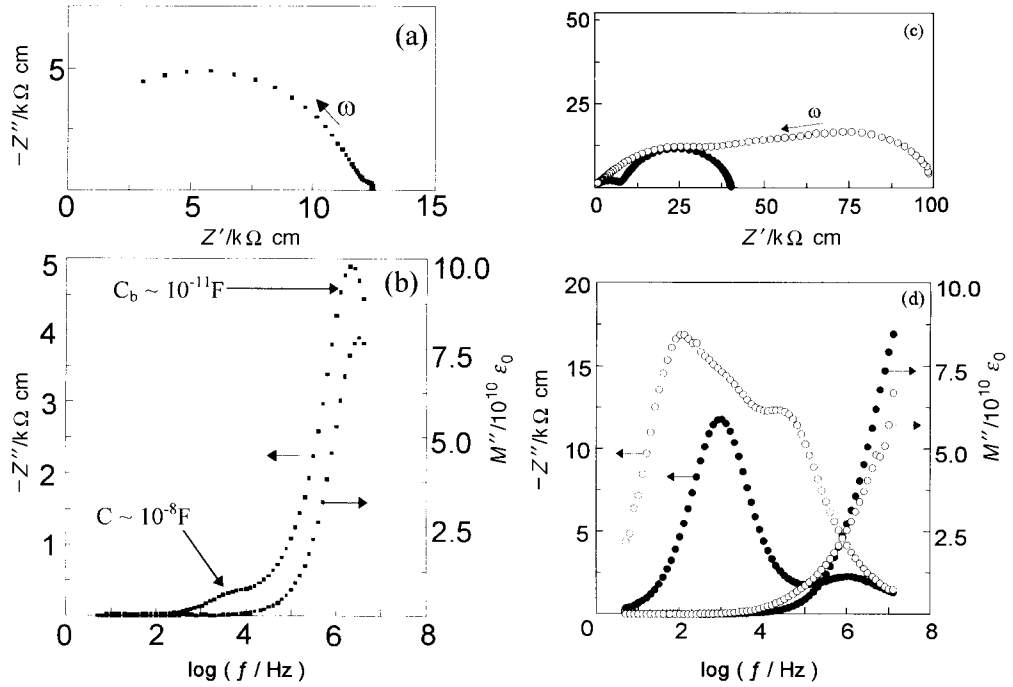

Fig. 6 (a) Complex impedance plane and (b) combined M'', Z'' spectroscopic plot at 252 K for Ca_2MnNbO_6, annealed in O_2 at 40 atm, 600 °C; (c) complex impedance plane and (d) combined M'', Z'' spectroscopic plot at room temperature for $Ca_2MnNbO_{5.87}$, quenched in air from 1400 °C; ● polished pellet, ○, unpolished pellet.

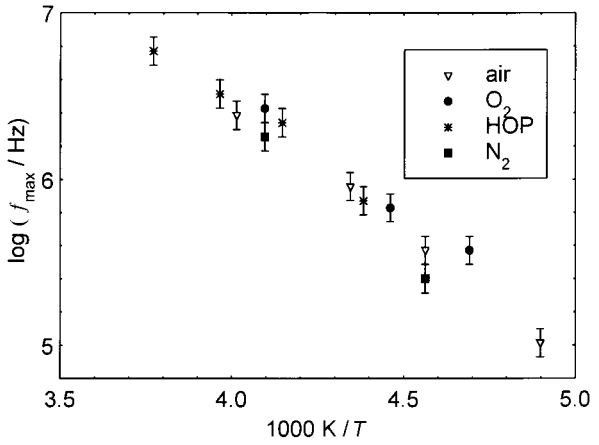

Fig. 7 Arrhenius plots of bulk (filled symbols) and total (open symbols) conductivities of Ca_2MnNbO_γ, prepared by different heat treatments; ■, □: slow cool from 1100 °C in nitrogen; ▼, ▽: quenched from 1400 °C in air; ●, ○: slow cool from 1100 °C in 1 atm oxygen; ▲, △: slow cool from 600 °C in 40 atm oxygen.

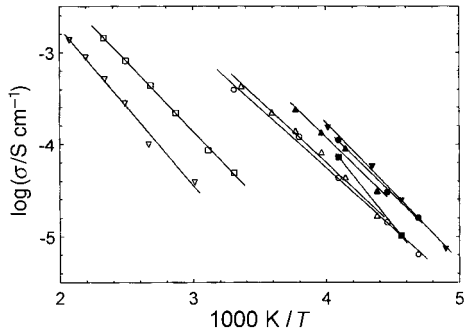

Fig. 8 Arrhenius plots of bulk (filled symbols) and total (open symbols) conductivities of Ca_2MnNbO_γ, prepared by different heat treatments: ■, □: slow cool from 1100 °C in nitrogen; ▼, ▽: quenched from 1400 °C in air; ●, ○: slow cool from 1100 °C in 1 atm oxygen; ▲, △: slow cool from 600 °C in 40 atm oxygen.

values which are almost independent of sample history. For pellets treated in O_2-rich atmospheres, the grain boundary resistance was relatively small and the total and bulk conductivities are almost coincident, Fig. 8. For the samples treated in air or N_2, however, very large grain boundary resistances are evident, Fig. 6(c), (d), and these dominate completely the pellet conductivities. In such O_2-poor atmospheres, the samples lose O_2 from their surfaces by the reaction

$$2O^{2-} \rightarrow O_2 + 4e$$

Since the surface/grain boundary conductivity decreases as a consequence, it is concluded that the conduction mechanism, in these regions at least, is p-type. The similarity in activation energy for the bulk and total conductivities in unreduced samples, Fig. 8 (slow cool from 1100 °C, 1 atm O_2 and from 600 °C, 40 atm O_2), indicates that a similar conduction mechanism occurs in both bulk and grain boundary regions and therefore that the bulk conductivity is also p-type. The insensitivity of the bulk conductivity to sample history indicates that the number of p-type carriers is high, associated with the high concentration of Mn^{3+} ions.

Conclusions

Ca_2MnNbO_6 has the orthorhombic $GdFeO_3$ structure. This is not surprising given the existence of similar structures in Ca_2FeNbO_6,[27] Sr_2CrTaO_6[28] and Pb_2ScNbO_6.[29] The similar sizes of Mn^{3+} and Nb^{5+} permit disorder of these elements over the octahedral B sites. Although Mn^{3+} is Jahn–Teller active, there is no evidence of distortions in the $(Mn,Nb)O_6$ octahedra, presumably because there is insufficient Mn present to exert a cooperative distortion.

The possible existence of oxygen vacancies in the $GdFeO_3$ structure is often speculated upon but is not well documented. Here, we find oxygen contents as low as 5.87 in samples heated at high temperatures and in atmospheres of low oxygen partial pressure. We believe that the oxygen content may be reduced further on H_2 reduction, although in fully reduced (to Mn^{2+} at $\gamma = 5.50$) samples, the products are multiphase and therefore,

the oxygen content can not be reduced as low as 5.50; further work on this is in progress.

The defect structure in the oxygen-deficient samples is not known, but it must involve reduction in coordination of some of the $(Nb,Mn)O_6$ octahedra. NbO_6 octahedra are not easily reduced and oxygen loss may, therefore, be confined to the MnO_6 octahedra, as occurs with $CaMnO_3$ which exhibits a coordination number of 5 for Mn on oxygen loss. Interestingly, it is difficult to fully oxygenate Ca_2MnNbO_γ and an oxygen content of 6.00 is achieved only under high oxygen pressures; this may reflect a reluctance of the Jahn–Teller active Mn^{3+} ion to occupy an octahedral site that is constrained to be undistorted by the adjacent NbO_6 octahedra.

Ca_2MnNbO_γ provides another example of spin glass-like behaviour, similar to that seen in A_2FeXO_6: A = Ca, Sr, Ba; X = Nb, Ti, Sb.[21–25] It is a p-type hopping semiconductor with an activation energy, 0.31 eV, that is largely independent of oxygen content and appears to be associated with the Mn^{3+} ions that are present in high concentration. In reduced samples, there appears to be preferential oxygen loss from sample surfaces and grain boundaries, as evidenced by a dramatic decrease in conductivity in these regions. This is probably because the concentration of Mn^{3+} ions is greatly reduced, in favour of Mn^{2+} ions, and hence the p-type carrier concentration is small. The bulk of the samples is largely uninfluenced by this effect (although the conductivity of the sample heated in N_2 is reduced, which may signal the outset of a significant reduction in p-type carrier concentration in the bulk for this sample). Whilst it is widely accepted that oxidation/reduction processes generally commence at surfaces, the present material provides a particularly clear example of the oxygen concentration gradients that must often occur; this effect is readily apparent here because of the sensitivity of the electrical properties to the degree of reduction.

References

1 B. A. Boukamp, M. P. van Dijk, K. J. de Vries and A. J. Burggraaf, *Adv. Ceram.*, 1987, **23**, 447.
2 G. Bronoel, J. C. Grenier and J. Reby, *Electrochim. Acta*, 1980, **25**, 1015.
3 J. C. Grenier, M. Pouchard and P. Hagenmuller, *Solid State Chem., Proceedings of the Second European Conference, Veldhoven*, ed. J. Schoonman, Elsevier, Amsterdam, 1982, p. 247.
4 S. Shin, Y. Hatakeyama, K. Ogawa and K. Shimomura, *Mater. Res. Bull.*, 1979, **14**, 133.
5 A. Atkinson, *Adv. Ceram.*, 1987, **23**, 3.
6 F. A. Kroger, *The chemistry of the imperfect crystal*, North-Holland, Amsterdam, 1964.
7 G. G. Libowitz, *Prog. Solid State Chem.*, *2*, Pergamon Press, Oxford, 1965.
8 C. N. R. Rao, J. Gopalakrishnan and K. Vidyasagar, *Indian J. Chem. A*, 1984, **23**, 265.
9 B. C. Tofield and W. R. Scott, *J. Solid State Chem.*, 1974, **10**, 183.
10 C. N. R. Rao, A. K. Cheetham and R. Mahesh, *Chem. Mater.*, 1996, **8**, 2421.
11 R. Mahesh, K. R. Kannon and C. N. R. Rao, *J. Solid State Chem.*, 1995, **114**, 294.
12 R. Portier, A. Carpy, M. Fayard and J. Galy, *Phys. Status Solidi A*, 1975, **30**, 683.
13 M. Hervieu, F. Studer and B. Raveau, *J. Solid State Chem.*, 1977, **22**, 273.
14 K. Scheunemann and H. K. Muller-Buschbaum, *J. Inorg. Nucl. Chem.*, 1975, **37**, 1875; 2261.
15 J. Berggren, *Acta Chem. Scand.*, 1977, **25**, 3616.
16 J. C. Grenier, M. Pouchard and P. Hagenmuller, *Structure Bonding*, 1981, **47**, 1.
17 K. R. Poeppelmeier, M. E. Leonowitz and J. M. Longo, *J. Solid State Chem.*, 1982, **44**, 89.
18 K. R. Poeppelmeier, M. E. Leonowitz, J. C. Scalon, J. M. Longo and W. B. Yelon, *J. Solid State Chem.*, 1982, **45**, 71.
19 J. A. Chavez-Carvayar, T. C. Gibb and A. R. West, *J. Mater. Chem.*, 1996, **6**, 1957.
20 S. Geller and E. A. Wood, *Acta Crystallogr.*, 1956, **9**, 563.
21 R. Rodríguez, A. Fernández, A. Isalgué, J. Rodríguez, A. Labarta, J. Tejada and X. Obradors, *J. Solid State Phys.*, 1985, **18**, L401.
22 T. C. Gibb, P. D. Battle, S. K. Bollen and R. J. Whitehead, *J. Mater. Chem.*, 1992, **2**, 111.
23 T. C. Gibb, *J. Mater. Chem.*, 1993, **3**, 441.
24 T. C. Gibb, A. J. Herod and N. Peng, *J. Mater. Chem.*, 1995, **5**, 91.
25 P. D. Battle, T. C. Gibb, A. J. Herod, S.-H. Kim and P. H. Munns, *J. Mater. Chem.*, 1995, **5**, 865.
26 J. T. S. Irvine, D. C. Sinclair and A. R. West, *Adv. Mater.*, 1990, **2**, 132.
27 J. A. Chavez-Carvayar, PhD Thesis, Aberdeen, 1995.
28 G. Patrat, M. Brunel and F. DeBergevin, *J. Phys. Chem. Solids*, 1976, **37**, 285.
29 F. Galasso and W. Darby, *Inorg. Chem.*, 1965, **4**, 71.

Paper 8/04865G